Characterization of geothermally relevant structures at the top of crystalline basement in Switzerland by filters and gravity forward modelling

Yassine Abdelfettah,[1,2] Eva Schill[2] and Pascal Kuhn[3]

[1]*Centre of Hydrogeology and Geothermics - CHYN, University of Neuchâtel, Neuchâtel CH-2000, Switzerland. E-mail:* yassine.abdelfettah@unine.ch

[2]*Institute of Nuclear Waste Disposal, Karlsruhe Institute of Technology KIT, D-76021 Karlsruhe, Germany*

[3]*Eidgenössisches Departement für Verteidigung, Bevölkerungsschutz und Sport VBS armasuisse Bundesamt für Landestopografie swisstopo Landesgeologie Seftigenstrasse 264 CH-3084 Wabern*

SUMMARY

Some of the major geothermal anomalies in central Europe are linked to tectonic structures within the top of crystalline basement, which modify strongly the top of this basement. Their assessment is a major challenge in exploration geophysics. Gravity has been proven to be suitable for the detection of mainly large scale lithological and structural inhomogeneities. Indeed, it is well known and proven by different wells that, for example, in northern Switzerland extended negative anomalies are linked to such structures. Due to depth limitation of wells, there vertical extension is often unknown. In this study, we have investigated the potential of gravity for the geometrical characterization of such basement structures. Our approach consists in the combination of the series of Butterworth filters, geological modelling and best-fitting between observed and computed residual anomalies. In this respect, filters of variable wavelength are applied to observed and computed gravity data. The geological model is discretized into a finite element mesh. Near-surface anomalies and the effect of the sedimentary cover were eliminated using cut-off wavelength of 10 km and geological and seismic information.

We analysed the potential of preferential Butterworth filtering in a sensitivity study and applied the above mentioned approach to part of the Swiss molasses basin. Sensitivity analyses reveal that such sets of residual anomalies represents a pseudo-tomography revealing the distribution of different structures with depth. This finding allows for interpreting negative anomalies in terms of 3-D volumes. Best-fitting then permits determination of the most likely 3-D geometries of such basement structures. Our model fits both, geological observations and gravity: among 10 deep boreholes in the studied area, six reach the respective units and confirm our distribution of the negative (and positive) anomalies.

Key words: Numerical solutions; Gravity anomalies and Earth structure; Crustal structure.

1 INTRODUCTION

Gravity and magnetics have proven to provide valuable evidence on the distribution of large-scale inhomogeneities in the crystalline basement in general (Edel 2004; Edel & Schulmann 2009) and information with respect to geothermal anomalies on regional (e.g. Baillieux *et al.* 2013) and local level (e.g. Guglielmetti *et al.* 2013). Major heat flow anomalies in central Europe are linked to hydrothermal convection in fractured crystalline basement (Illies & Greiner 1979; Kohl *et al.* 2000; Pribnow & Schellschmidt 2000; Bächler 2003). Kohl *et al.* (2000) and Bächler (2003) have shown that the convection occurs along fault zones related to the tectonics of the Upper Rhine valley. This convection accounts to a large part (about 75–85 per cent) for the temperature anomalies of these

geothermal fields and its pathways are reflected in negative gravity anomalies (Baillieux *et al.* 2013). In a similar way, structural elements in the basement of the Swiss Molasse basin revealing naturally enhanced permeability may contribute to the surface heat flux anomaly pattern. A 2-D thermohydraulic modeling for the area of Bad Zurzach (Rybach *et al.* 1987) has revealed a strong influence of deep thermal water up-flow along the Northern boundary fault of late-Variscan graben structures, that is Permo-Carboniferous troughs in the granitic basement. Indeed a contribution of thermal fluid from the Permo-Carboniferous is also assumed for the geothermal reservoir of Riehen (Schill & Klingler 2010, and references therein).

In general, seismic tomography appears to be a successful tool to detect geothermal anomalies in volcanic environment (e.g. Muksin
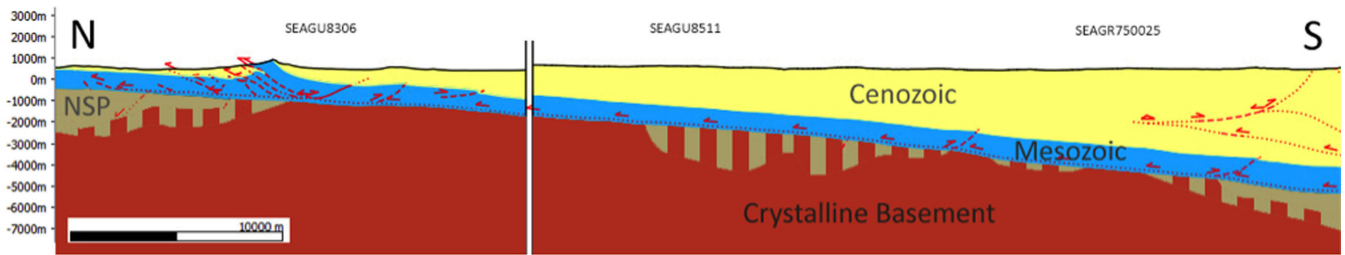
Figure 1. Sketch of the geological interpretation of the seismic section TS10 from the seismic atlas of Switzerland (Sommaruga *et al.* 2012). Grey areas mark the Permocarboniferous troughs that are confirmed by deep wells such as the North Swiss Permocarboniferous trough (NSP). Striped areas indicate Permocarboniferous troughs that are classified 'possible' or 'of unknown extension'.

et al. 2013). Although low velocity zones coincide with geothermal reservoirs, their identification and characterization in the basement requires sophisticate methods such as, for example 3-D shear wave tomography (Calò *et al.* 2013) and remains a challenge in exploration geophysics. The nature of seismic reflectors within the crystalline basement remains the subject of inference except where reflections have been traced directly to outcrop (Klemperer 1987). To a first approximation, acoustic impedance variations in sedimentary basins are controlled by velocity changes, whereas velocity and density can vary independently in the crystalline crust and changes in density may be relatively more important in controlling reflectivity. In certain instances, density fluctuations outweigh velocity fluctuations (Gough 1986). With this in mind, gravity has been proven to be an excellent parameter to investigate big-scale inhomogeneities at the top of the basement and in particular, to be a good exploration tool for the investigation of Permo-Carboniferous troughs in Switzerland. Indeed, it was this method that permitted the first interpretation on the extension of the Northern Swiss trough (Klingelé & Schwendener 1984). Further Permo-Carboniferous troughs, however, have been investigated by seismic methods, only (e.g. Gorin *et al.* 1993; Sommaruga *et al.* 2012). A summary of the challenges in localization of Permo-Carboniferous trough structures using seismic data (Marchant *et al.* 2005) reveals a number of different geological features that may account for observed weak reflection.

The remaining difficulties are comprehensible, for example in the 'Seismic atlas of the Swiss Molasse Basin' (Sommaruga *et al.* 2012) and illustrated for a representative example from the study area in Fig. 1. On 16 seismic lines across the entire Swiss molasses basin a total lateral extension of about 465 km of the basement has been labelled 'possible' Permo-Carboniferous trough identified by seismic reflection in the basement and a total of 995 km are labelled 'uncertain extension', identified by intermediate reflection. About 100 km of Permo-Carboniferous trough of the possible Permo-Carboniferous is confirmed by the wells Entlebuch-1 and Weiach-1. Thus, these established criteria provide indication for Permo-Carboniferous, but need to be combined with further available information in order to establish whether or not Permo-Carboniferous deposits are present.

The aim of this study is to develop an exploration concept for the geometry of the top basement. This has been approached using a preferential high- and bandpass Butterworth filter (Butterworth 1930) on gravity data to investigate the geometry, the thickness of the Permo-Carboniferous grabens and thus, the depth of crystalline basement. Since filtering or continuation of potential field data may introduce itself artefacts under certain geometries (e.g. Sailhac *et al.* 2000), its potential was analysed in a sensitivity study. The identified bodies were furthermore verified using 3-D

gravity forward modelling on the basis of a finite element mesh. The Permo-Carboniferous troughs were selected as test structures due to their relevance for geothermal systems and shale gas plays in Switzerland (Schill *et al.* 2012) and the expected significant signal with respect to other inhomogeneities in the Swiss crystalline basement. An additional aim of this study is to improve the knowledge on the spatial and vertical distribution, as well as the internal structure of the Permo-Carboniferous graben in Northern Switzerland.

2 GEOLOGICAL SETTING AND PETROPHYSICS OF THE BASEMENT

The crystalline basement underneath the Alpine Molasse basin has experienced a multistage tectonic evolution. Among major structures are several typically ESE–WNW striking graben structures, the so-called Permo-Carboniferous troughs. These basement grabens are widely spread across Europe (McCann *et al.* 2006) and origin in the Westphalian period, when thermally induced doming evolved into crustal extension and resulted in a series of pull-apart basins (Mann *et al.* 1983). About 265 Ma intense transtension induced wrench faulting and syntectonic sedimentation of the lower fan series into the Permo-Carboniferous troughs (Diebold 1990; Ziegler 1990). A detailed analysis of the depositional environment is described from the boreholes in Weiach, Riniken and Benken (Blüm 1987; Matter 1987). The Permo-Carboniferous period is characterized by the sedimentation in the following environments: anastomosing fluvial systems (Stephanian), alluvial fans (Saxonian), lacustrine systems in the early Permian (Autunian) and playa sediments in the late Permian (Oberrotliegendes; Blüm 1989). A peneplain with ongoing sedimentation marks the tectonic quiescence under a regional tensional setting in the early Mesozoic (Matter 1987; Ziegler 1992). The development of the Rhine graben system during Eocene and Oligocene caused a reactivation of the Permo-Carboniferous graben boundaries as steep normal faults (Ustaszewski *et al.* 2005). During Miocene uplift of the Black Forest is combined with an increased sedimentation in the Molasse basin (Ziegler 1992) and the formation of the Jura Mountains in the late Miocene. In this area, the formation of the Jura folds seems to be coupled with a partial tectonic inversion of the Palaeozoic basins localized in the core of an anticline (Laubscher 1965; Pfiffner 2009).

Permo-Carboniferous throughs are describe throughout central Europe from France (Ustaszewski *et al.* 2005) and western Switzerland (Gorin *et al.* 1993) across the Upper Rhine Graben (Schumacher 2002) and the Molasse basin (NAGRA 2008) to eastern Germany (Zeh & Brätz 2004). The best investigated

Permo-Carboniferous trough in Switzerland is the so-called North Swiss trough. In this region, the thickness of Permian sediments in the Upper Rhine Graben was first estimated using seismic and well information as well as palaeogeographic considerations (Boigk & Schöneich 1970, 1974). A first regional interpretation of the gravity data has shown a negative elongated anomaly. This anomaly has been interpreted quantitatively in terms of depth of the crystalline basement (Klingelé & Schwendener 1984). A residual has been obtained (Klingelé & Schwendener 1984) by subtracting the regional trend from the Bouguer anomaly, which was determined using a polynomial of third order and fitting their coefficients by least square. For the interpretation in terms of depth of the top crystalline, the reduction density of 2400 kg m^{-3} has been chosen due to the fact that the areas with Permo-Carboniferous troughs at depth are overlain by Quaternary sediments with a density close to that value.

From gamma-gamma logs a mean density of 2550 kg m^{-3} has been obtained for the Permo-Carboniferous deposits. This value has been confirmed by borehole gravity measurements. It implies a density contrast of 100 kg m^{-3} between the Permo-Carboniferous troughs and the crystalline basement (Klingelé & Schwendener 1984). A detailed review of the density measurements from adjacent boreholes reveals the origin of the contrast. Two effects are observed in different wells; not only the bulk, but also the particle density of the Permo-Carboniferous sediments is lower with respect to the crystalline rocks. The latter difference affects mostly the Permian playa and alluvial fan sediments, especially when they are composed of coarse grained sandstone. Density differences of up to 580 kg m^{-3} with a mean value of about 270 kg m^{-3} are observed, for example, in the well Weiach-1. In the same well, density differences up to 370 kg m^{-3} with a mean value of about 160 kg m^{-3} are observed for the Carboniferous anastomosing fluvial system as well as the lacustrine series. The crystalline basement in Weiach-1 is barely weathered and shows only small differences of about 90 kg m^{-3} (Matter *et al.* 1988a). Comparable values for the density and the density differences between grain and bulk rock can be found for the wells in Riniken (Matter *et al.* 1987), Kaisten (Peters *et al.* 1989b), Schaffisheim (Matter *et al.* 1988b) and Leuggern (Peters *et al.* 1989a). In Böttstein the mean density of the crystalline basement is of about 100 kg m^{-3} lower (Peters *et al.* 1986). This increased difference between grain and bulk density of the sediments, due to increased porosity and original material, implies a sufficient density contrast allowing their detection by gravity measurements.

3 GEOPHYSICAL APPROACHES

In this study, we have investigated systematically the application of high and bandpass Butterworth filters of different wavelengths using synthetic and measured data to detect and characterize the 3-D geometry of the top crystalline basement. The geometries obtained from a series of residual anomalies in the study area have been used as starting model for 3-D finite element gravity forward modelling (see below, Fig. 12c). Further constrained by additional geological, geophysical, and borehole information, the model has been refined in an iterative process to best-fitting the obtained set of residual anomalies. In this respect, the same post-processing (i.e. Bouguer filtering) has been applied to the forward model Bouguer anomaly.

Butterworth filters were applied to complete Bouguer anomalies. They are controlled by two parameters: (1) the cut-off frequency (or wavelength) and (2) the filter order. Artefacts such as the appearance of overestimated anomalies by interpolation a series of smaller and aligned anomalies are detected using the signal from short wavelength filters. Since in the Swiss Molasse basin, the Bouguer anomaly is mainly dominated by the gravity effect of the geometry of the Molasse sediments deepening towards the Alps, this regional trend is eliminated using a long wavelength filter to visualize basement structures. Following the observations from the sensitivity study, that is increasing filter wavelength visualizes increasing larger or deeper structures, we have used different wavelength to (i) delineate and characterize different (negative) anomalies at depth, and (ii) build a pseudo-tomography using high- and bandpass filters. Moreover, the filter order parameter can be also changed to delineate a very small variation, for instance, in the case of low density contrast between the Permo-Carboniferous trough and the basement. With increasing filter order the horizontal density contrast is emphasized. This will be the focus of a forthcoming paper.

3-D gravity data sets were generated from the different models with a homogeneous basement density of 2670 kg m^{-3}. Forward modelling was achieved using Pohanka's algorithm (Pohanka 1988) applied to a finite element model. In this algorithm, vertical gravity attraction is computed by

$$g(r, \varepsilon) = -G\delta \sum_{k=1}^{K} n_k \sum_{l=1}^{L(k)} \Phi_{k,l}$$

with

$$\Phi_{k,l} = \phi(U_{k,l}(r), V_{k,l}(r), W_{k,l}(r), z_k(r), \varepsilon)$$

and where **r** is the distance between the gravity station and the element, G is the gravitational constant, δ is the density of the element (or density contrast), $\mathbf{n}_k$ is the normal vector to the surface k formed by l edges. **U**, **V** and **W** are the geometrical function in the x, y and z directions. The value ϵ is an infinitesimal number to avoid some singularities; it is $\leq 10^{-6}$ and represents only 1 μGal in the gravity anomalies. Uncertainties on the computed gravity values Δg_ϵ can be assessed by

$$\Delta g_\varepsilon = |g(r, \varepsilon) - g(r)| \leq 5G|\delta|\varepsilon \sum_{k=1}^{K} L(k),$$

where $g(r)$ is the exact gravity value. The computed gravity values $g(r, \varepsilon)$ are bounded by the quantity $\pm\Delta g_\epsilon$. This formula can also be used to assess the value of ε according to the desired uncertainties. A detailed description of the algorithm is provided in Pohanka (1988).

Discretisation of the 3-D models was carried out using the 3-D finite element mesh generator Gmsh (version 2.5.1; Geuzaine & Remacle 2009). This meshing allows for approaching the real geological geometries using tetrahedrons. However, due to considerable regional consistency of the sedimentary layers, a simplified geology of the study was created directly in Gmsh for the geometry of the sedimentary layers of the Molasse basin. The 3-D geological modelling of the basement structures was carried out using MOVE® (Midland valley). As initial model a simple, irregular triangle mesh with a vertex distance of 0.2–5 km was created based on seismic information in order to trace the top of the crystalline basement s.s., that is without Permo-Carboniferous structures. The triangulated surfaces were discretized into a tetrahedron finite element model with a cell size of about 500 m using TetraVolume. The final model was obtained by gravity forward modelling and iterative manual adaptation of the initial model.

4 SENSITIVITY ANALYSES OF PREFERENTIAL BUTTERWORTH FILTER

A detailed sensitivity analysis of preferential Butterworth filters (Abdelfettah & Schill 2013) using a synthetic finite element model is summarized in the following. Special focus is given to the possible basement inhomogeneities.

A synthetic finite element model ($70 \times 80 \times 10$ km^3) has been built using a representative 25×25 m digital elevation model resampled to 1×1 km with elevation between 173 and 3020 m. The model incorporates six 3-D volumes at different depth and of different shape, representing structural elements expected in the Swiss subsurface (Fig. 2). All these volumes are embedded into a synthetic geological model representing the geological setting in the Swiss Molasse basin (Fig. 2) including the Molasse sediments at the top (Cenozoic), two layers of Mesozoic sediments in intermediate depth, and the crystalline basement at the bottom. A regional dip from north to south is assigned to the Mesozoic sediments causing an increase in thickness of the Cenozoic sediments. In the following, we will describe the test volumes and explain the particular interest in each of them.

The volumes B1 and B6 represent typical Quaternary deposits. They are used to investigate, if their gravity effects can be distinguished by the applied filters from the effects of underlying structures and thus, removed. Volume B6 is additionally characterized by an eastward dipping bottom and a vertical plane on its eastern boundary. It is mainly used to investigate the differences from the deep volumes that are equally expected to cause long wavelengths. Volume B2 may represent a lithological change in the basement such as crystalline intrusions. Volume B3 represents a structure of small thickness and low angle dip, such as a fault with possible fracture porosity of a few percent. This is used to test the robustness of the Butterworth filter. The volumes B4 and B5, two separate bodies, occur on top of each other and at significant but different depth. It should be mentioned that volumes B1 and B6 occur in the Cenozoic formation. B2 to B5 may be found and crosscut different formations down to the basement. For the simulation of Bouguer anomaly, representative density values from the Swiss Molasse basin and were attributed to the respective geological units (Table 1).

Simulation of Bouguer anomaly of the synthetic, geologic 3-D finite element model is shown in Fig. 3(a); it reveals a decreasing Bouguer anomaly due to increasing sediment thickness. The volumes B1 to B6 appear according to their depth and difference in density to the geological layers as well-outlined anomalies. Representative examples of the residual anomalies resulting from high- and bandpass Butterworth filtering using different frequencies (10,

Table 1. Density values assigned for each geological unit for the 3-D geological model showed in Fig. 2, and used in the sensitivity study of the Butterworth filter.

| Formation name	Density (kg m^{-3})
Cenozoic	2500
Upper Mesozoic	2550
Lower Mesozoic	2600
Crystalline basement	2670
B1	2400
B2	2620
B3	2600
B4	2600
B5	2600
B6	2400

20, 30, 35 and 50 km high-pass and 20–50 and 40–100 km bandpass wavelength) are presented in Figs 3(b)–(h).

The 10 km high-pass Butterworth filter (Fig. 3b) reveals obvious geometrical outlines for the near-surface anomalies B1 and B6. The dynamic range of the residual anomalies ranges between 0.31 and –0.32 mGal and regional trend observed in the Bouguer anomaly appears to be removed completely from the anomaly. The quality of the outline of the anomalies B4 and the eastern, shallower part of B3 as well as the top of B2 is reduced with respect to the original outline of the volume. The deep parts of B2 are not recognized in their full extension, whereas B5 is clearly not identified.

With increasing wavelength of the filter towards higher values, the dynamic range increases successively up to 2 mGal and the absolute values increase to -2.8 mGal for the 50 km filter wavelength. Increasing wavelength sharpens the geometric outline of the shallow volumes B1 and B6 as well as the deeper parts of B2 and B3. A separation between B4 and B5 cannot be achieved from the isoline plot using the given range of wavelength. Cutting-off high frequencies (Fig. 3d), the accuracy of the outline of the shallow volumes decreases with increasing lower wavelength and the contribution from the deep parts of the volumes becomes more prominent. This is evident, for example, for B5. A separation between B4 and B5 is still not evident from the isoline plot. In order to emphasize the potential in determination of the geometry of the volumes using pseudo-tomography, we present eight 2-D profiles through the volumes for the following filters: 10, 20 and 30 km high-pass and 20–50 and 40–100 km bandpass filters. The lines A-B, C-D, to, O-P (Fig. 3) show the localization of the extracted 2-D sections presented in Fig. 4.
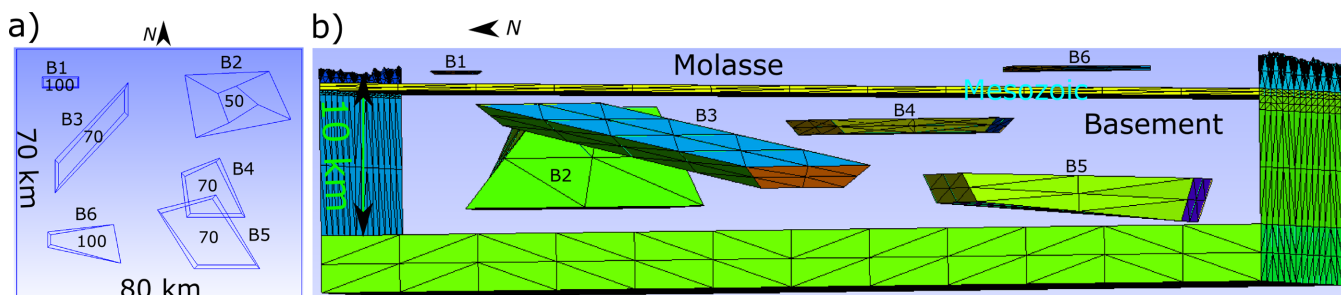
Figure 2. Finite element discretization of the synthetic 3-D geological model used in the sensitivity study of the preferential Butterworth filter showing the geometry and distribution of the investigated volumes B1–B6 (see in the text) in top view (a) and in a view from the west (b). Numbers indicate the applied negative density contrast for each body in kg m^{-3} during forward modelling.
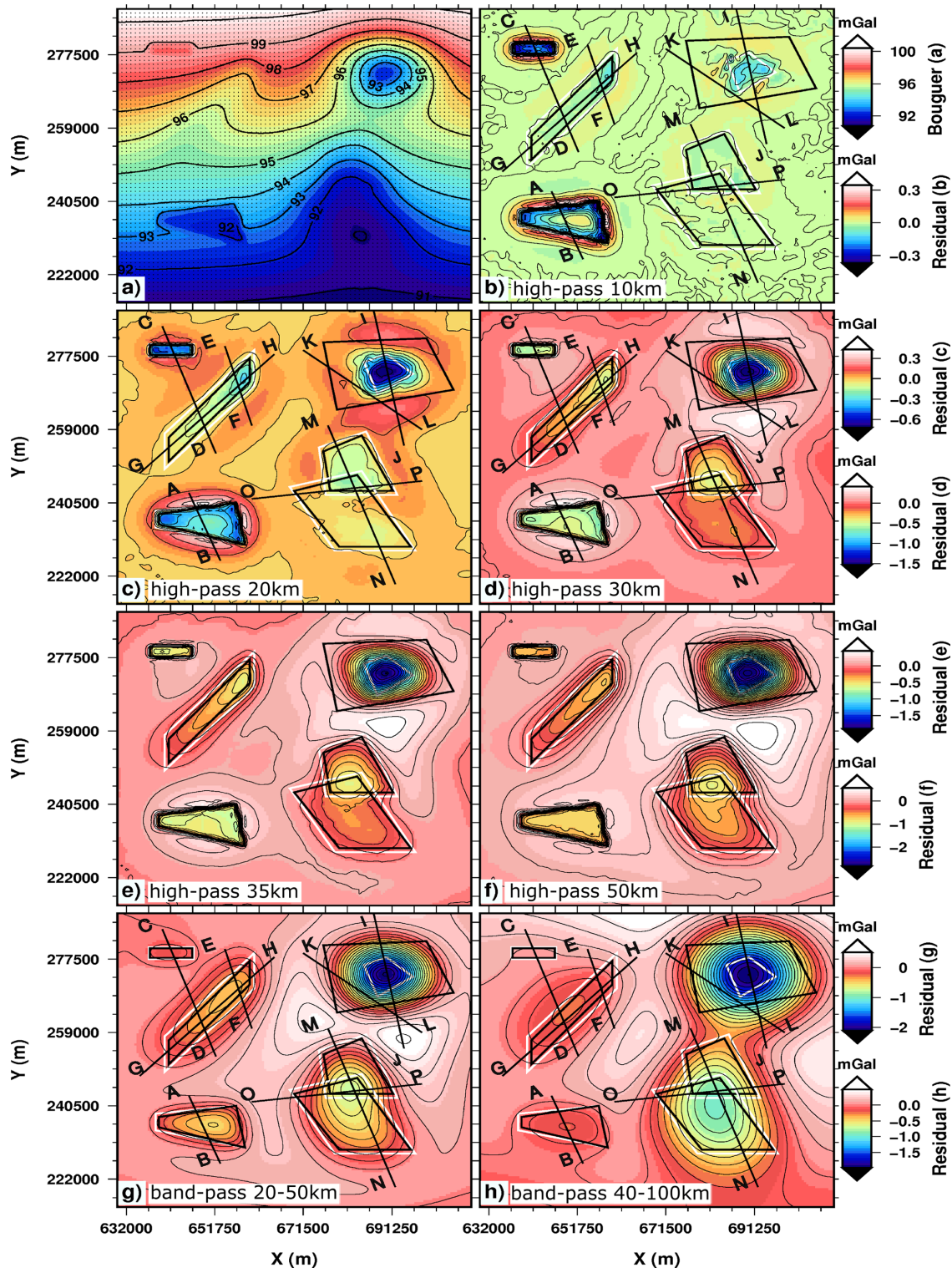
Figure 3. Bouguer and residual anomalies calculated from the synthetic 3-D geological model (Fig. 2) using density values from Table 1. (a) Bouguer anomaly, (b)–(f) residual anomalies obtained with high-pass Butterworth filters of 10, 20, 30, 35 and 50 km wavelength, respectively, (g) and (h) residual anomalies obtained using bandpass Butterworth filter of 20–50 and 40–100 km wavelength, respectively. Lines A-B, C-D, to, O-P indicate the extracted 2-D sections presented in Fig. 4. The *X*–*Y* geometry of the volumes B1–B6 is shown by white (extension at top) and black lines (extension at bottom).

From Fig. 4 (A-B and C-D cross-sections), we may conclude that Quaternary sediments can be located and well delimited in their extension using short-wavelength high-pass filters. Bandpass filters may be used to erase the majority of their contribution to the gravity signal, since they are not of geothermal significance.

The sections I-J and K-L cross the volume B2 in the middle and at a lateral position, respectively. Starting from a wavelength of 20 km, the amplitude increases continuously with increasing maximum wavelength for both profiles with the exception of the amplitude of the bandpass filter 40–100 km for the cross-section
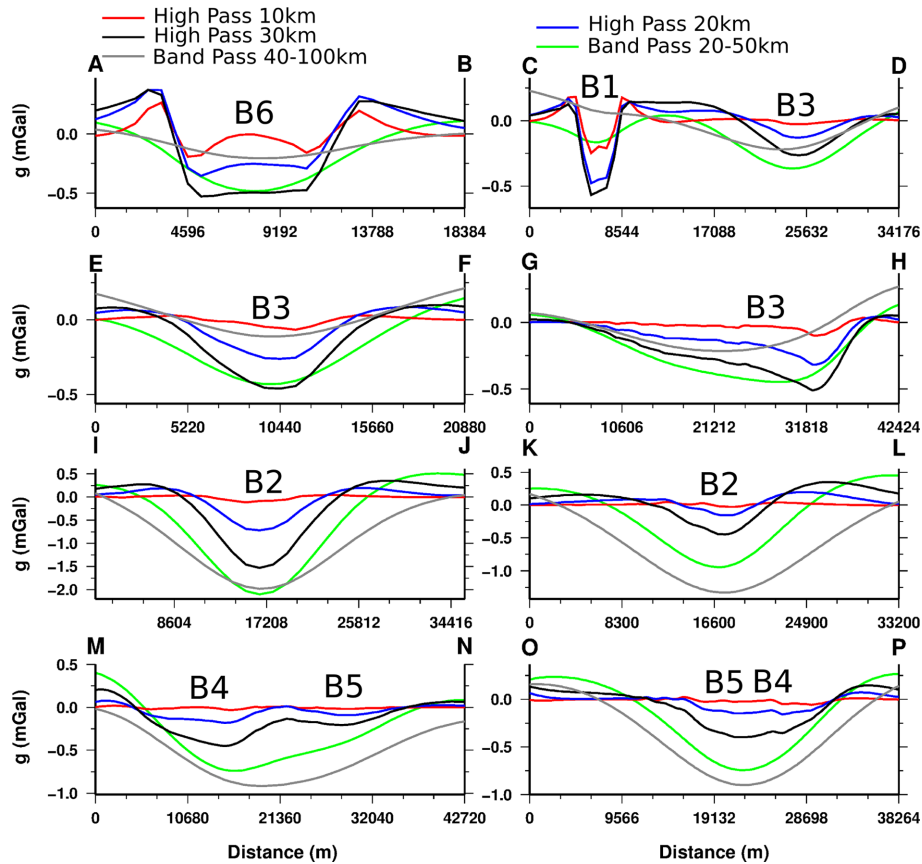
Figure 4. Eight representative 2-D cross-sections extracted from the residual anomalies showed in Fig. 3.

I-J. This is comparable to the 20–50 km bandwidth, which means that the bottom of B2 is reached in I-J. The dynamic range of the residual anomalies for the central cross-section I-J is twice the one of the lateral profile K-L. The general increase in amplitude is more prominent for the central position and in particular for the high-pass filters with shorter wavelength. The shallowest part of the volume in the central part of the volume B2 is affected by the 40–100 km bandpass filter causing a reduction in amplitude with respect to the 20–50 km filter. Our observations demonstrate that this type of geometry can be assessed using different wavelength.

Geometrically the above-discussed profile I-J reveals similarities with the profile E-F cross-cutting the thin inclined volume B3. The dynamic range of the residual anomaly, however, is four times larger in I-J. The effect of inclination is clearly visible in the profile G-H by its asymmetry as well as in the relative amplitudes in the profiles C-D and E-F, in particular for the bandpass wavelength of 40–100 km. As expected, differences between the bandpass and high-pass filters are largest at the shallow part of the volume.

As described above, the separation of the two volumes B4 and B5 is a challenge, since they appear as single anomaly in the isoline plots of all filters (Fig. 3). Indication of two distinct volumes can be found applying the high-pass 20 and 30 km filters. This becomes more evident in the profile M-N, in which the amplitude of the two filters is larger for B4, which is located at shallower depth compared to B5. The low amplitude on the B5 volume in these filters as well as the lateral shift in the maximum negative amplitude of the bandpass filters towards B5 indicates that this volume creates a contribution to the residual anomaly from greater depth.

In conclusion, we observe that the large-scale variation in the basement lithology can be geometrically described in detail at their

top and with acceptable accuracy at their bottom using high-pass and bandpass filters, respectively. Fault zones in the basement with shallow inclination can be described geometrically as well, when a density contrast ranges in the order of about 70 kg m^{-3}. This corresponds to fracture porosity in the fault zone of a few percent. Such fault zones can offer fluid pathways for hydrothermal circulation. Our sensitivity study shows that wavelength dependent Butterworth filtering in combination with 3-D forward modelling based on finite element discretized geological models is a powerful tool to locate and comprehend those structures in their 3-D extension. In the following, we will demonstrate that results from real data in a test area in Northern Switzerland confirm our observations in the sensitivity study.

5 RESULTS FROM THE CENTRAL MOLASSE BASIN OF SWITZERLAND

5.1 Results from Butterworth filtering of gravity data

The Bouguer anomaly of the central part of the Swiss Molasse basin with a reference density of 2670 kg m^{-3} (Fig. 5a) shows the typical decrease in gravity mainly due to increasing subsidence of the basin towards the Alps as well as to deepest continental structure of the collision zone. Residual anomaly obtained using high pass filter with a wavelength $\lambda = 20$ km (Fig. 5b) evidences the effect of mainly Cenozoic (i.e. Quaternary) sediments striking preferentially NNW–SSE in the southern and central part of the study area and ENE–WSW at the transition to the Jura Mountains (Figs 5c and d). Some of gravity effects especially in the northeastern part of the
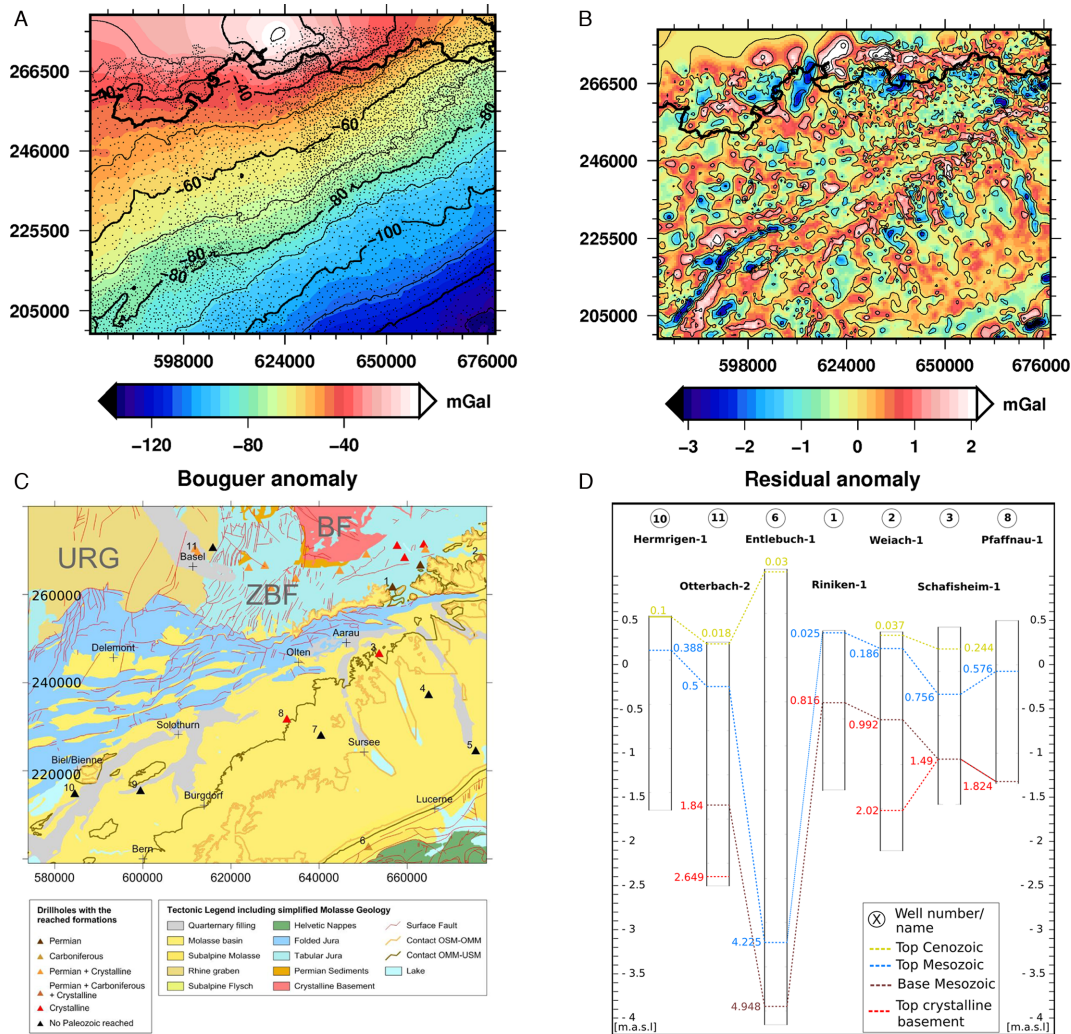
Figure 5. (a) Observed Bouguer anomaly available in the Gravimetric Atlas of Switzerland. As expected from the known geological structures, the regional Bouguer anomaly trend is strongly dominated by the gravity effect of the Molasse basins as well as deepest structures. Dots show gravity measurement localization. Panel (b) show the residual anomaly obtained using 20 km high pass Butterworth filter wavelength, where 2 mGal isovalues were showed. This residual anomaly shows mainly the quaternary filling of the different basins as well as heterogeneities, which may occur in the Molasse. (c) Tectonic map (Swisstopo 2005b) of the studied area (URG, Upper Rhine Graben; BF, Black Forest; ZBF, Zeininger Bruch Field) with additional Molasse-information extracted and adapted from the geological map (Swisstopo 2005a). The major deep wells show the distribution of the drilled basement formations. (d) Well correlation chart showing the major deep wells used for the interpretation of the Permo-Carboniferous distribution (depth to top layers is indicated). 1: Riniken-1, 2: Weiach-1, 3: Schafisheim-1, 6: Entlebuch-1, 8: Pfaffnau-1 and 11: Otterbach-2.

study area (Jura Mountains) may be attributed to heterogeneities in the Mesozoic sediments such as near-surface karstification.

In the following, we will present the residual gravity anomalies using different sets of bandpass filters using either a variable longer wavelength and fixed shorter wavelength limit of 10 and 20 km in Figs 6 and 7, respectively, or variable shorter and fixed longer wavelength limit of 70 km in Fig. 8. Since the sensitivity analysis clearly revealed a link between decreasing wavelength limit and depth, our way of data analysis represents a pseudo-tomography. This is illustrated, for example, for the shallow subsurface by the difference in the size of the anomalies, representing negligible near-surface influence in Fig. 7. Pseudo-tomography is used in this study with special focus on determining the depth of the crystalline basement underneath the Permo-Carboniferous grabens. This is mainly obtained from the long wavelength limit of 70 km in Fig. 8. For comparison to our results for the deep subsurface, the lithology in existing boreholes is provided in Fig. 5(d).

Cutting-off wavelengths <10 km, reveals major positive and negative anomalies between 2 and –3 mGal (e.g. AN1–AN5, Fig. 6). With respect to the near-surface structures (Fig. 5b) the strike of the anomalies changes to E–W mainly in the northern part of the study area and to nearly NE–SW in the southern part. Generally, the amplitudes of both, negative and positive anomalies increase with increasing a maximum cut-off wavelength. This indicates comparably deep structures, since the increasing wavelength of filters represents anomalies originating from greater depth. However, while the half width of the negative anomalies typically increases, it appears to be less variable for positive anomalies. There are some exceptions from this general pattern. The negative anomaly AN1 located north of Bienne (Fig. 6), for example, shows no significant increase in amplitude or half width at increasing maximum cut-off wavelength between 30 and 60 km. Furthermore, the positive anomaly AN2 located about 10 km to the south of well 11 reveals a decrease in amplitude with increasing maximum cut-off wavelength
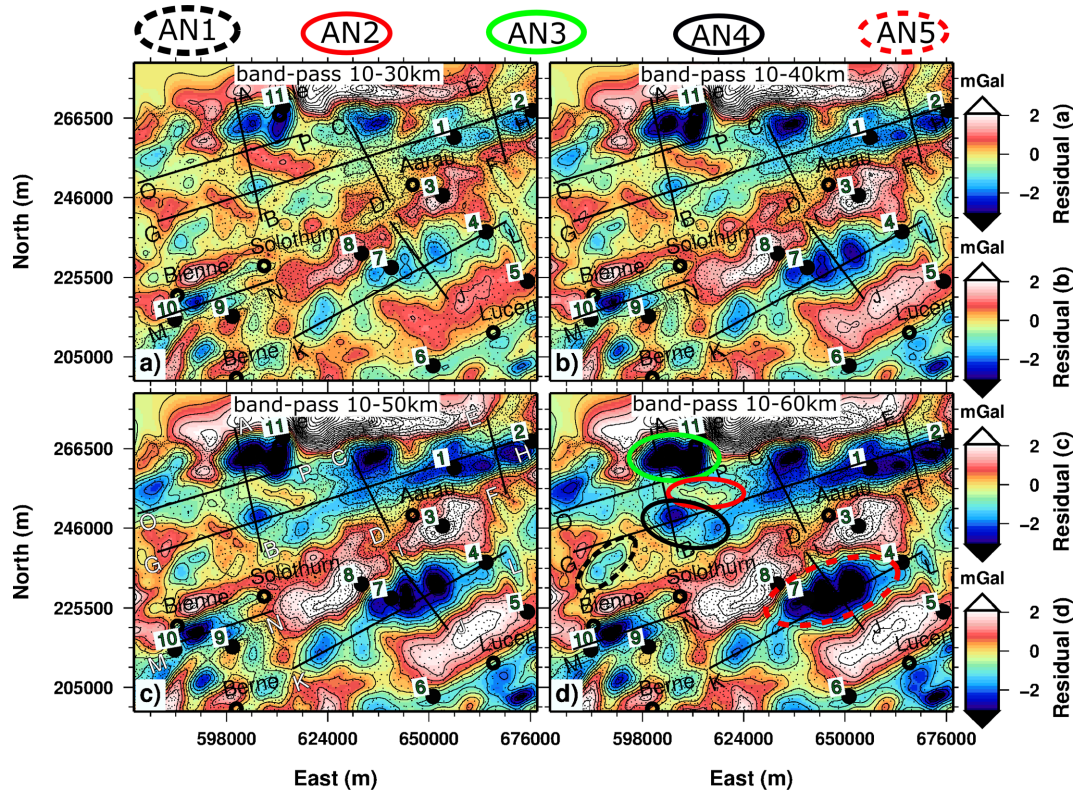
Figure 6. Application of Butterworth filter on observed Bouguer anomaly to northwestern side of Switzerland. Panels (a)–(d) show residual anomalies obtained using 10–30, 10–40, 10–50 and 10–60 km bandpass Butterworth filter, respectively where isolines of 1 mGals were superimposed. These residuals give us a 'pseudo tomography' with depth. The principle is to keep constant the shorter wavelength limit (i.e. 10 km) and increase the longer wavelength limits from 30 to 60 km, to assess and quantify the continuity of structures at depth. Numbers 1 to 11 show the localization of the deep boreholes existing in the studied area. Lines A-B, C-D, to, O-P show the localization of the extracted 2-D cross-sections illustrated in Fig. 9.

(Figs 6a–d) confirming the broadening of surrounding negative anomalies related to deep structures.

Generally, a comparison of the observations with litho-logs from 12 different wells distributed across the study area (Figs 5c and d) shows that positive anomalies are linked to wells in which the crystalline basement is overlain directly by Mesozoic sediments, for example Schafisheim and Pfaffnau (Matter *et al.* 1988b), whereas in areas of negative anomalies Permo-Carboniferous graben fillings are observed, for example Weiach, Riniken, Otterbach and Entle-buch (Matter *et al.* 1987, 1988a; Vollmayr & Wendt 1987; Häring 2001).

In the following, we will discuss the results with respect to the horizontal and vertical continuity. The horizontal continuity of the E–W and NE–SW aligned negative anomalies appears to be stable with increasing maximum cut-off wavelength. As mentioned above most of the increase in amplitude and half width with depth occurs in the negative anomalies. In contrast, positive anomalies show comparably stable width with increasing depth (Fig. 6). This shows that the negative anomalies represent a continuing density contrast at depth, that is continuity of the Permo-Carboniferous structures at depth.

In order to study the vertical continuity of the anomalies, we start from a minimum cut-off wavelength of 20 km (Fig. 7). This allows to nearly completely suppressing the effect of the near surface anomalies. We would like to mention here that the general long wavelength pattern observed throughout Fig. 7 is consistent with the results using a minimum cut-off wavelength of 10 km (Fig. 6). As shown above, differences in amplitude increase from a maximum

cut-off wavelength of 30–60 km and are observed again in particular for negative anomalies. Consistently with Fig. 6, the negative anomaly AN1 reveals smallest increase in amplitude.

These general differences in the continuity of the various anomalies are nailed down using additional filters in Fig. 8 along different profiles (indicated in Figs 6 and 7). The profiles confirm that variation with different filters is typically larger in the negative anomalies. An approximate 2-D symmetry is observed for the deep bodies on the profiles A-B, E-F, I-J and K-L (Fig. 9). Profile A-B and the central part of G-H are good examples for the variable contribution from different depth levels to the minimum anomalies. While the northern anomaly AN3 (A-B) shows only moderate increase in amplitude with depth, AN4 seems to represent a deeper lying structure since significant amplitude can be observed in both 20–80 and 40–80 km filters in profile G-H. Largest amplitudes and largest increase with depth is observed for anomaly AN5 on profile I-J and K-L. We interpret this as an important and deep rooting structure. A good example of asymmetry can be observed in profile C-D, where the minimum shifts with increasing maximum cut-off wavelength towards the south indicating deepening of the structure towards that direction.

In order to investigate the differences in maximum horizontal and vertical length of the structures, we have applied a stable maximum cut-off wavelength of 70 km and minimum cut-off wavelengths of 20, 30, 40 and 50 km (Fig. 8).

As expected from the deepening of the Molasse and Mesozoic sediments towards the Alps, in the small minimum cut-off wavelength filter strongest minima are observed in the northern part of the
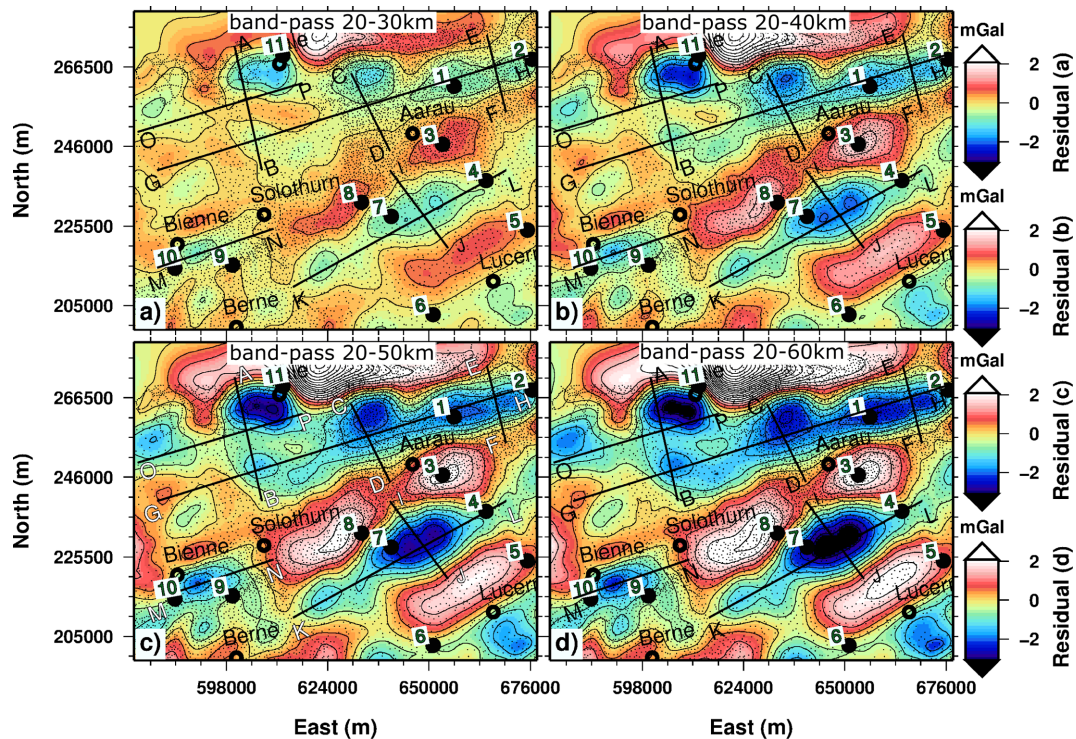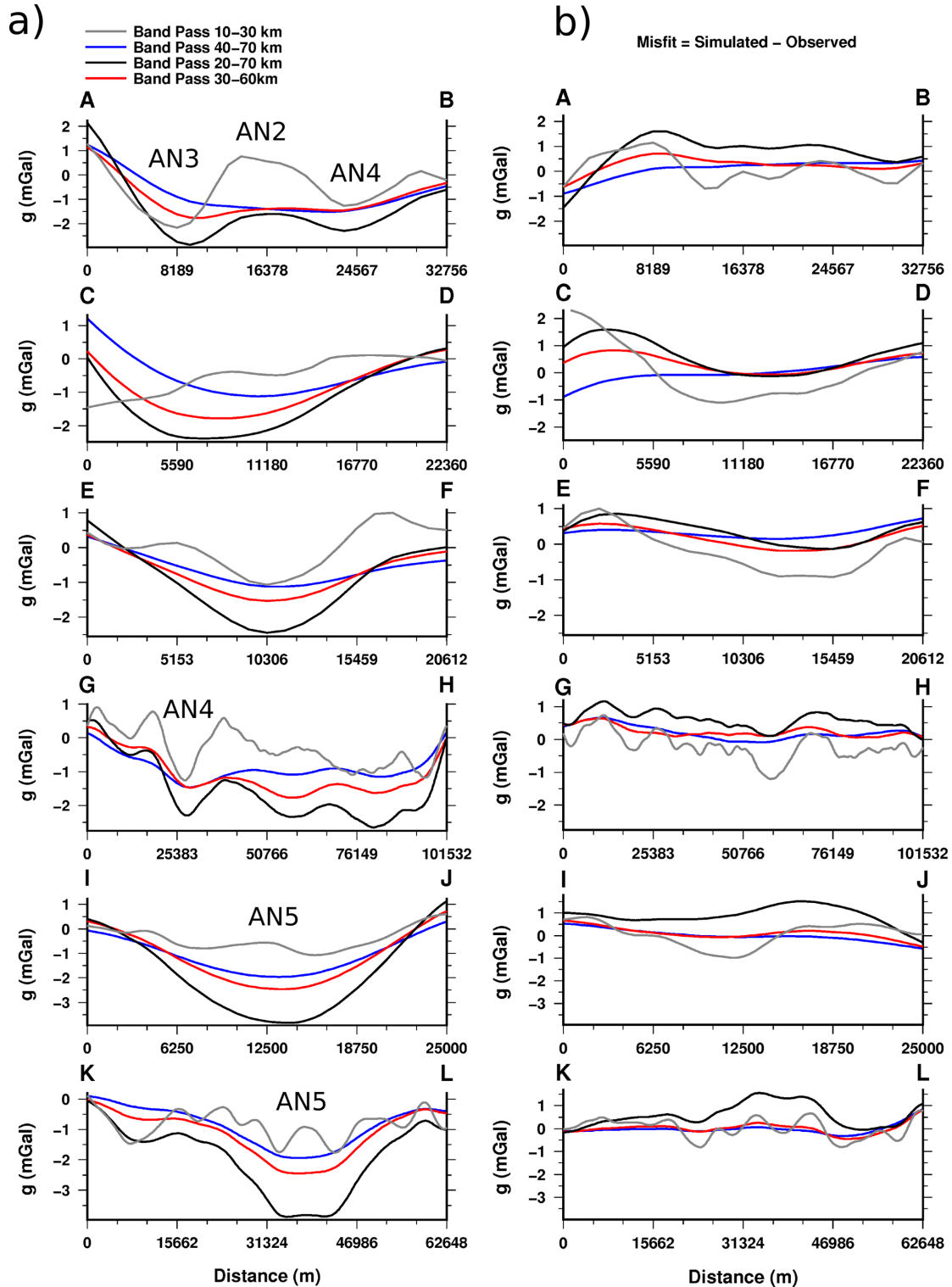
Figure 7. Residual anomalies obtained from Bouguer anomaly showed in Fig. 5(a) using bandpass Butterworth filter of (a) 20–30 km, (b) 20–40 km, (c) 20–50 km and (d) 20–60 km wavelengths, respectively. Isolines of 1 mGal were superimposed. The same approach as that used in Fig. 6 was followed, where the shorter wavelength limit was set constant to 20 km. Lines A-B, C-D, to, O-P show also the localization of the extracted 2-D cross-sections presented in Fig. 9.
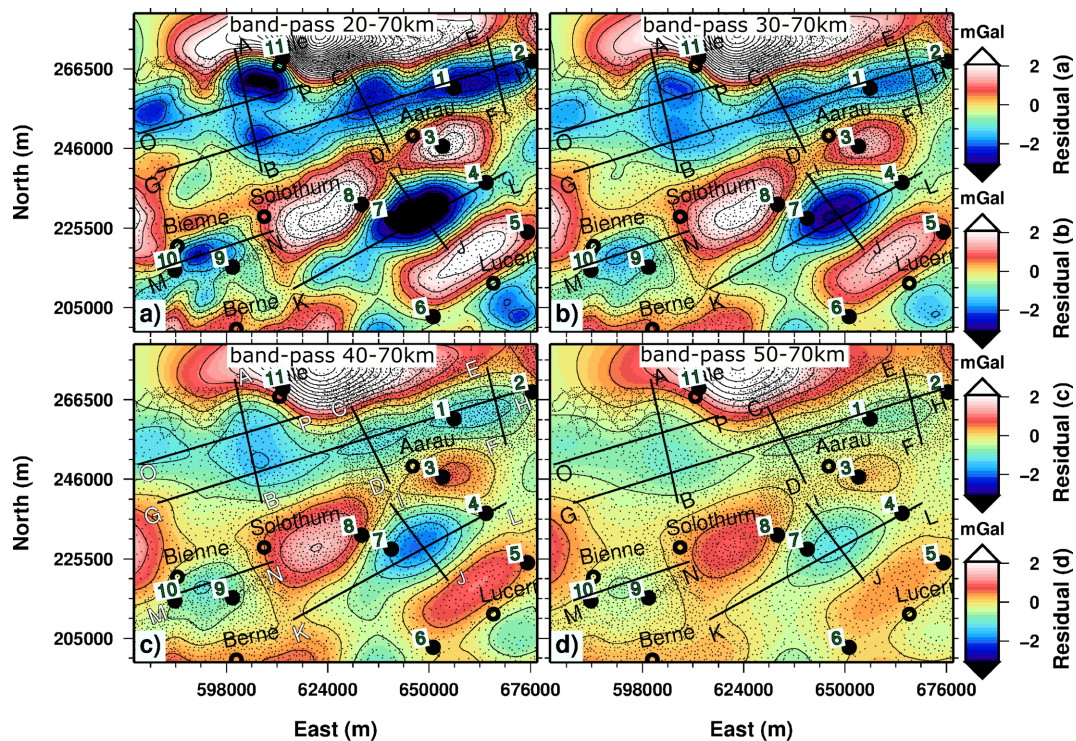
Figure 8. Residual anomalies obtained from Bouguer anomaly using bandpass Butterworth filter of different wavelengths; (a) 20–70 km, (b) 30–70 km, (c) 40–70 km and (d) 50–70 km, respectively. The isolines are equal to 1 mGal. Inversely to Figs 6–7, we set constant the longer wavelength limit at 70 km and increase the shorter limits. This approach, and in complement to previous results, shows the decreasing of the anomalies with depth.

Figure 9. (a) 2-D cross sections extracted from observed residual anomalies showed in Figs 6–7. (b) Misfit between six representative observed residual anomalies and simulated responses obtained from proposed geological model (Fig. 12a) for different bandpass wavelength. In general, we can observe that the misfit does not exceed 0.5 mGal, which is a good results working in regional scale. See the text for more details.

study area, where the top crystalline basement is expected at comparatively shallow depth. It should be mentioned here that anomaly AN5 is an exception since it is equally prominent with respect to AN3, although the top graben is located at large depth. However, in general, the first anomaly fading away with increasing minimum

cut-off wavelength is AN1. As observed in the 10-x and 20-x filters, this is suspected to be the least deep of all negative anomalies in the study area. With respect to its high negative anomaly in the small minimum cut-off wavelength filters, also anomaly AN3 seems to be comparably shallow. At a minimum cut-off wavelength of 50 km
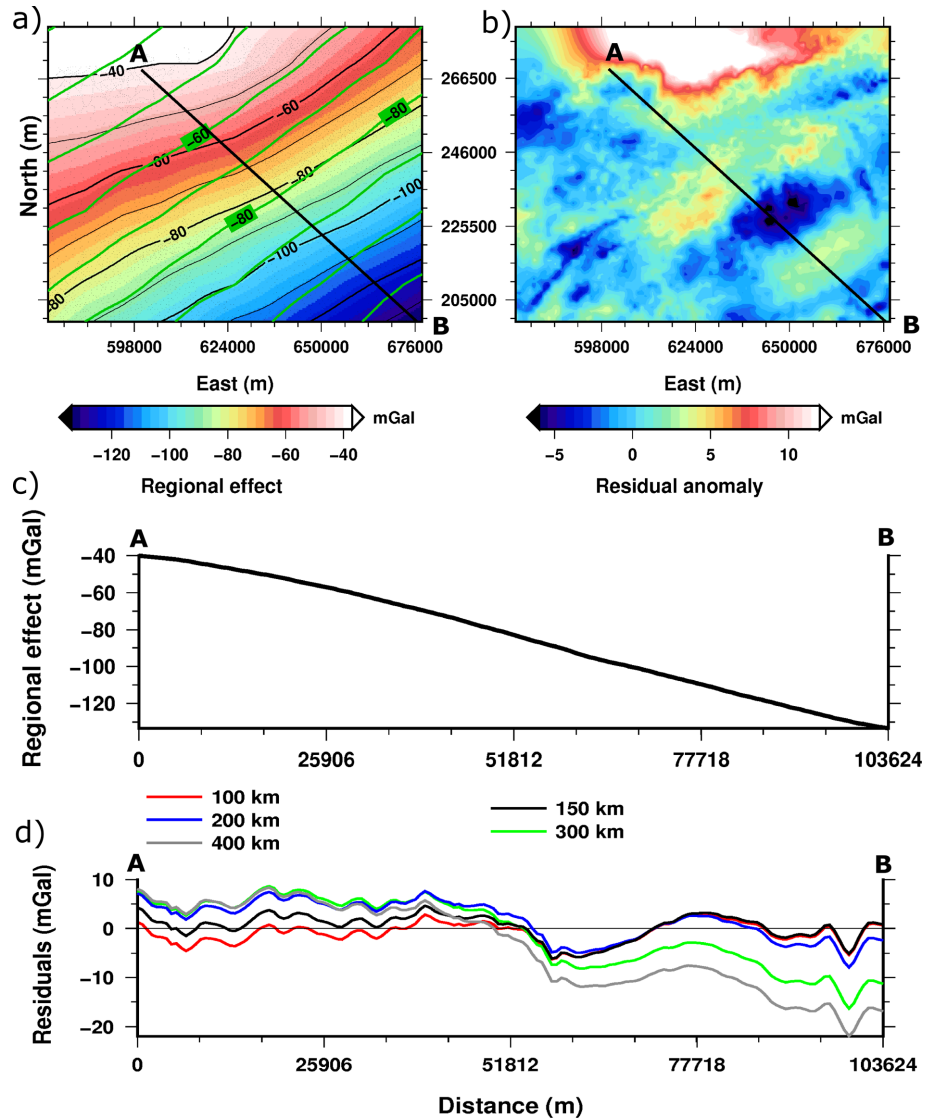
Figure 10. The classical approach used to assess and remove the regional trend, which masks the complete Bouguer anomaly. (a) Two representative regional trends computed by low pass filters using wavelengths of 150 km (black isolines) and 400 km (green isolines). The black dots show the location of the gravity stations. (b) Residual anomaly obtained using high pass filter using wavelength of 150 km. (c) 2-D cross section of the regional trend computed in (a) using low pass $\lambda = 150$ km. (d) Show different residual anomalies computed using high pass Butterworth filters extracted in the same location, that is A-B. The regional effect is well removed using high pass filter of 100 and 150 km, after this threshold a gravity regional effect is not well resolved as we can observe with those obtained by wavelength >150 km. Moreover, the regional gravity trend changes the orientation as can observed in panel (a).

(Fig. 8d) both, the prominent series of anomalies in the northern part of the study area and the anomaly south of Bienne reveal negative residual anomalies of about –1 mGal. Anomaly AN5 is to be discussed in more detail since it is the largest one in the study area and persists throughout all filters. From the x-70 filters it appears to be the deepest rooting anomaly (Fig. 8). This pattern is again consistent with the general geological setting as mentioned above. The shallow low density response shown in Fig. 6 is expected to be related to other effects in the sedimentary cover. It is well known, for example, that in the area of the sub-Alpine folded Molasse enhanced pressure gradients occur, representing hydrocarbon reservoir zones (Müller *et al.* 1988).

The possibility to investigate the upper limit of the observed structures has been tested using 10, 20 and 30 km high pass filters. However, since the influence from upper lying Quaternary and Molasse sediments cannot be fully excluded (see below), this

approach will be tested in a forthcoming paper using 3-D seismics as a reference.

In conclusion, we would like to emphasize that to this point our analyses reveal a number of stable minimum gravity anomalies originating from structures in the crystalline basement that persist throughout a certain depth range. In comparison, classical approaches such as assessing one best-fitting regional trend, only, as well as down- or upward continuation or derivatives, result in one best-fitting residual anomaly (Fig. 10). In our case, determination of a single regional trend ignores the change in orientation of the regional trend with depth as showed in Figs 10(a) and (c). A conventional high-pass filtering is shown in Figs 10(b) and (d), revealing small wavelengths dominating the residual anomaly. Consequently, to interpret the deeper structures, these shallower effects, generally provided from sediments, should be accurately modelled.

5.2 Gravity forward modelling based on finite element model

The correlation between boreholes reaching the crystalline basement s.l., that is including the Permo-Carboniferous graben fillings, and gravity anomalies (Figs 5–7) indicates strongly that the 'deep' structures observed in this preferential Butterworth analysis generally represent graben and horst structures formed at the end of the Variscian orogeny. In order to support our geometrical interpretation of these structures, we have performed a 3-D geological model of the area of investigation, discretized the model in a finite element model and calculated its gravity response as well as its residual anomalies applying the same filters presented above.

5.2.1 Set-up of the 3-D geological model

A geological 3-D model of the study area was set up with a vertical extension ranging from 2000 m depending on the local topography to –10 000 m above sea level. Surface topography has been obtained from Digital Elevation Model of 25 m (Swisstopo 2005c). The following simplification of the geology of the sedimentary cover was made respecting the general geological setting known from, both, seismic results (Nagra 2008; Sommaruga *et al.* 2012) and well data (Fig. 5d; Matter *et al.* 1987, 1988a,b; Vollmayr & Wendt 1987; Häring 2001): (1) Cenozoic sediments fill the volume between top Mesozoic and topography. (2) At the top basement, Mesozoic sediments have been modelled with a constant thickness of 900 m and dipping with approximately 2° to the SE. These assumptions originate from the re-interpretation of 14 seismic sections across the entire Swiss molasses basin of Sommaruga *et al.* (2012, Fig. 1). Due to the complex geology the Neogene graben structure of the Upper Rhine valley has not been included in detail in the model. A high resolution 3-D geological model has been evaluated in combination with gravity by Schill & Klingler (2010), revealing a strong link between negative anomalies and Permo-Carboniferous troughs underneath the Upper Rhine Graben as well. In this study, the Permo-Carboniferous graben fillings have been generally modelled using four surfaces. Their top (type surface TS1) is represented by the base of the Mesozoic sediments, while the bottom includes the bottom of the shoulder (TS2), typically filled with Permian sediments only, and the bottom of the deep Permo-Carboniferous graben (TS3). Lateral boundaries (TS4) represent steep boundary faults (Fig. 11). The base of the Mesozoic sediments as well as its top was set constant in the 3-D geological model according to the surrounding available well data.

### 5.2.2 Gravity forward modelling of the basement structures

An iterative approach has been used to fit observed and modelled gravity data using an overall minimum misfit of the residual anoma-

Table 2. Density values assigned for each geological unit to achieve gravity forward modelling of the proposed 3-D geological model.
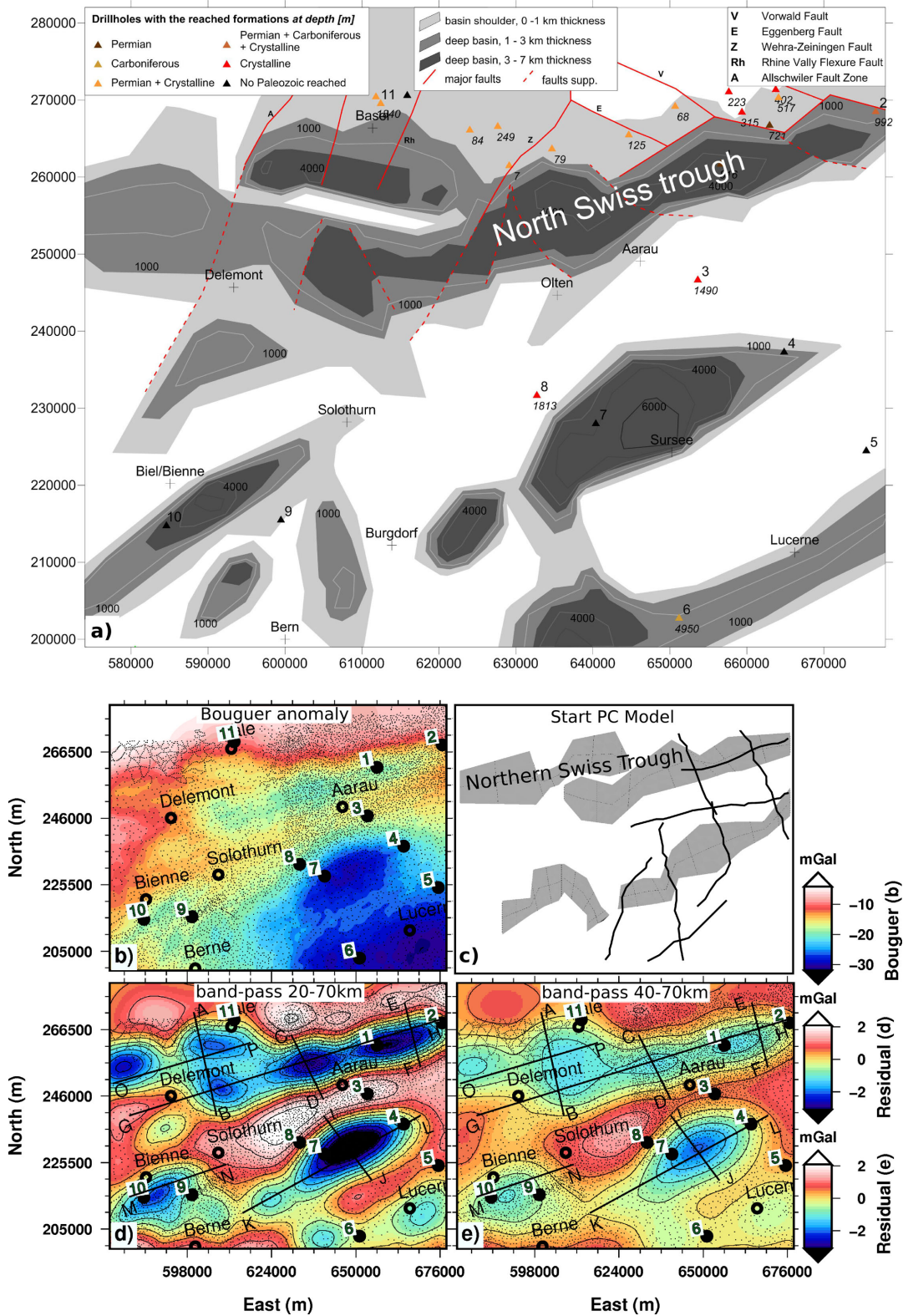
Geological formation	Density (kg m^{-3})
Cenozoic	2500
Upper Mesozoic	2550
Lower Mesozoic	2600
Crystalline basement	2670
Permo-Carboniferous troughs	2570

lies. The misfit analysis includes all filters used in the present study with wavelengths >20 km in order to avoid the signal of the Quaternary deposits. In this process boundaries simplified from borehole and seismic data down to the base of the Mesozoic sediments as well as densities are fixed to the initial geometry and values (Table 2), respectively. Thus, the only variable is the geometry of the basement structures. The simplified geology of the sedimentary cover is supported by the analysis of the residual anomalies revealing deep seated structures to be the origin of the negative anomalies. The density distribution from the wells in the study area has been analysed to determine mean density values for the simulation of the gravity response of the different volumes of the 3-D geological model (see chapter 2 and Table 2). High variability in density is observed for the Cenozoic sediments as well as for the Permo-Carboniferous fillings. The latter vary between 2210 and 2620 kg m^{-3} resulting in a mean density of 2415 kg m^{-3}, for example density log in the Weiach-1 borehole (Matter *et al.* 1988a), whereas a variation between 2430 and 2740 kg m^{-3} with a mean value of 2700 kg m^{-3} is observed for the crystalline basement. Despite this important mean density contrast of −285 kg m^{-3}, a significantly more conservative value of −100 kg m^{-3} has been used in this study. This may lead to a partial overestimation of the size of the Permo-Carboniferous structures mainly their thicknesses.

The resulting interpretation of the Permo-Carboniferous structures of the study area is shown in Fig. 12(a). Representative examples of residual anomalies (bandpass between 20–70 km and 40–70 km) obtained from forward modelling of the gravity response of the geological finite element model are presents in Figs 12(d) and (e). Comparison with the residual anomalies obtained from observed data (Figs 7 and 8) reveals that they are in good general agreement. It should be mentioned that in particular in the 20–70 km filter, the amplitudes and the shape of the positive anomalies could not be reproduced by the geological finite element model, because we modelled only the low density anomalies. Representative misfits are presented along four profiles across different negative anomalies (Fig. 9), and compared to the original filtered data. The misfit varies generally around ± 0.5 mGal compared to minima of up to about −2.5 mGal. Best fits are obtained along the ENE–WSW trending
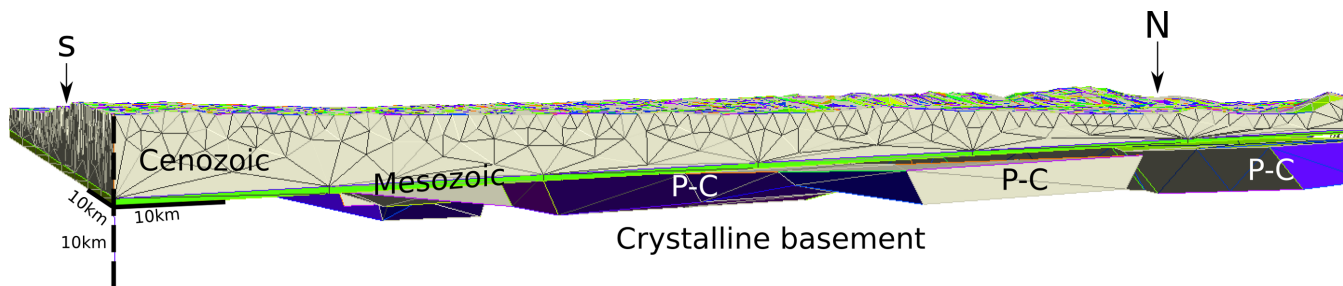
Figure 11. Example of geometries and finite element meshing of the simplified geological model used to assess the gravity effect of the Permo-Carboniferous grabens in the crystalline basement.

Figure 12. (a) Geological interpretation from the forward gravity model of the distribution of the Permo-Carboniferous troughs in the studied area derived mainly from qualitative and quantitative gravity interpretations constrained by seismic and existing geological and fault interpretation (e.g. Nagra 2008), as well as borehole information (well references in the text), using simplified geological structures. Well labels see Fig. 5; the depth to the basement is indicated in italic. (b) Computed Bouguer anomaly form 3-D geological model including Permo-Carboniferous grabens. (c) Horizontal distribution of the Permo-Carboniferous graben in the initial model, where continuous lines show the location of 2-D seismic lines used to constrain the model. This figure could be directly compared to (a), where differences can be observed in many locations (e.g. south of Basel, south of Delemont and Biel). Panels (d) and (e) show simulated residual anomalies obtained on the final 3-D model using 20–70 and 40–70 km bandpass filter, respectively. These anomalies can be compared directly to those shown in Figs 8(a) and (c).

profiles parallel to the axes of the structures at gravity minima (G-H, K-L). This may indicate that the general depth and lateral extension of the Permo-Carboniferous structures are well traced. Larger variation is observed along the perpendicular profiles (A-B, I-J). On profile A-B major misfit is observed in the part where the profile cuts the important positive anomaly in the northern part of the study area that is linked to the southern Black Forest massif. Nevertheless, also for anomaly AN3 (minimum residual anomalies of about -0.75 to -2.5 mGal), we still observe a misfit of $\pm$ 1 mGal. On the one hand this unsatisfactory misfit of the negative anomaly may be caused by our choice to simplify the structures of the Upper Rhine Graben, on the other hand there is a special geological features, the so-called Zeininger Bruchfeld, which is characterized by important faulting and high fracture density.

6 DISCUSSION AND CONCLUSION

It is well known that filter analysis applied to potential field data may create misleading large anomalies if, for example, small near-surface anomalies are grouped or aligned (see Blakely (1995) for more thorough review). If we supposed that is the case, these negative anomalies will be observed preferentially in the short wavelength residuals (e.g. <20 km). Thus, their gravity contribution will be important mainly in 10-$\times$ km bandpass and <20 km high pass, but will be strongly reduced in 20-$\times$ km bandpass. Cross-sections K-L (between $\sim$15 000 and $\sim$50 000 m) and G-H ($\sim$34 000 to $\sim$90 000 m) clearly show such behaviour. Moreover, our sensitivity analyses show clearly the link between wavelength of anomalies, cut-off wavelength of the used filter and depth of the buried body.

Our basement model is confirmed by all wells reaching the respective Permo-Carboniferous units or the basement (Fig. 12). The wells Riniken-1, Otterbach-2 and Entlebuch-1, located inside the negative anomalies, cross >980 and 809 m of Permian and 204 m of Permo-Carboniferous units, respectively. The well Weiach-1, located at the rim of this negative anomaly, reaches the crystalline basement after crossing 1028 m of the Permo-Carboniferous. The wells Schafisheim and Pfaffnau-1, located in the centre and at the rim of a positive anomaly, reach the crystalline basement directly below the Mesozoic sediments. During modelling, we have respected at the rim of the North Swiss trough the offsets caused by the conjugated Variscian faults striking in ENE–WSW and WNW–ESE direction from the Black Forest Mountains into the Molasse basin. The validity of this is confirmed, for example, by the decrease in misfit in the respective eastern part of profile G-H (Fig. 9).

In the following, we will shortly discuss our results with respect to the improvement of the knowledge on the local geology. As for the North Swiss trough, our model is in good agreement with the interpretation of Nagra (2008), both for the northern and southern boundaries. However, to the East of the Wehra-Zeininger fault, we expect the graben to be more important and to the West of this fault, we expect a graben that connects to the one south of Basel observed also by Schill & Klingler (2010) and Ustaszewski & Schmid (2007). In contrast to earlier interpretations, we observe no direct connection to the West of the Allschwiler fault as suggested by Ustaszewski & Schmid (2007). With a thickness of up to 7 km the ENE–WSW trending Permo-Carboniferous graben to the SW of the well Boswil-1 marks the thickest Permo-Carboniferous one in the study area. Southwest of the deep Altishofen basin a second minor basin. A shallow, up to 1.5-km-thick elongated basin trends from the well Entlebuch-1 to Lucerne and further to WNW. The graben systems in western part of our study area seem to be more complex

than assumed before. The Palaeozoic basin supposed in Hermrigen (Pfiffner *et al.* 1997) could be confirmed by the gravity data. Its northeastern border is interpreted to be in the area of Solothurn and its deepest part is located about 3 km SE of Biel.

In conclusion, we can state that the following steps have been achieved for the interpretation of gravity data:

(1) Butterworth filters with a variety of wavelengths emphasize a number of stable minimum and maximum gravity anomalies.

(2) The sensitivity study conducted on the Butterworth filtering showed that the gravity effect due to shallow structures can be separate from the one originating from deep basement structures. The combination of, mainly, the high and bandpass Butterworth filter and 3-D finite element forward modelling is an essential tool to characterize the extension of the bodies embedded in the crystalline basement at different depth.

(3) Constrained by borehole information the geological finite element model forward modelling of gravity and best fitting with observed residual anomalies reveals a distribution of the Permo-Carboniferous structures in the crystalline basement.

(4) Our model fits both, geological observations and gravity: Among ten deep boreholes in the studied area, six reach the respective units and confirm our distribution of the negative (and positive) anomalies.

(5) We proposed à new regional geological model where 3-D geometries of Permo-Carboniferous troughs were addressed. Our model agrees well with the previous interpretation on the occurrence of Permo-Carboniferous structures derived mainly from geology, seismics and borehole observations. It moreover provides insight into horizontal and vertical boundaries of the Permo-Carboniferous grabens. Their depth and thicknesses are also assessed using a negative density contrast of 100 kg m^{-3}. Some interesting features are also revealed in Northern Swiss Permo-Carboniferous trough, as AN2 horst, which separates this Permo-Carboniferous graben at north and south two branches.

REFERENCES

Abdelfettah, Y. & Schill, E., 2013. Exploration of geothermally relevant structures in the crystalline basement of Switzerland using gravity constrained by seismic data, in *Proceedings of the European Geothermal Congress,* EGC 2013, Pisa, pp. 1–9.

Bächler, D., 2003. Coupled thermal-hydraulicchemical modeling at the Soultz-sous-Forêts HDR reservoir (France), *PhD thesis,* Swiss Federal Institute of Technology, Switzerland.

Baillieux, P., Schill, E., Edel, J.-B. & Mauri, G., 2013. Localization of temperature anomalies in the Upper Rhine Graben: insights from geophysics and neotectonic activity, *Int. Geol. Rev.,* **55,** 1744.

Blüm, W., 1987. Diagenese permischer Schuttfächer—Sandsteine der Nordschweiz, *Eclogae geol. Helv.,* **80,** 369–381.

Blüm, W., 1989. Faciesanalyse im Rotliegenden des Nordschweizer Permokarbon-Trogs (Hochrhein-Region zwischen Basel und Laufenburg), *Eclogae geol. Helv.,* **82,** 455–489.

Boigk, H. & Schöneich, H., 1970. Die Tiefenlage der Permbasis im nördlichen Oberrheingraben, in *Proceedings of the International Rift Symposium Graben Problems,* eds Illies, J.H. & Müller, S.E., Schweizerbart'sche, Karlsruhe.

Boigk, H. & Schöneich, H., 1974. Perm, Trias und älterer Jura im Bereich der südlichen Mittelmeer-Mjösen-Zonen und des Rheingrabens, in *Proceedings of the International Rift Symposium: Approaches to Taphrogenesis,* eds Illies, J.H. & Fuchs, K., Schweizerbart'sche, Karlsruhe.

Butterworth, S., 1930. On the theory of filter amplifiers, *Wireless Eng.,* **1,** 536–541.

Calò, M., Kinnaert, X. & Dorbath, C., 2013. Procedure to construct three-dimensional models of geothermal areas using seismic noise cross-correlations: application to the Soultz-sous-Forêts enhanced geothermal site, *Geophys. J. Int.,* **194**(3), 1893–1899.

Diebold, P., 1990. Die tektonische Entwicklung der Nordschweiz, *Nagra informiert,* **90,** 47–55.

Edel, J.B., 2004. Structure et évolution du Fossé Rhénan, du Carbonifère à nos jours—apports de la géophysique, *Bulletin de la société d'histoire naturelle et d'éthnographie de Colmar,* **65,** 21–50.

Edel, J.B. & Schulmann, K., 2009. Geophysical constraints and model of the "Saxothuringian and Rhenohercynian subductions— magmatic arc system" in NE France and SW Germany, *Bulletin de la Société Géologique de France,* **180,** 545–558.

Geuzaine, C. & Remacle, J.-F., 2009. Gmsh: a three-dimensional finite element mesh generator with built-in pre- and post-processing facilities, *Int. J. Numer. Methods Eng.,* **79**(11), 1309–1331.

Gorin, G.E., Signer, C. & Amberger, G., 1993. Structural configuration of the western Swiss Molasse basin as defined by reflection seismic data, *Eclogae geol. Helv.,* **86,** 693–716.

Gough, D.I., 1986. Mantle upflow tectonics in the Canadian Cordillera, *J. geophys. Res.: Solid Earth,* **91,** 1909–1919.

Guglielmetti, L., Comina, C., Abdelfettah, Y., Schill, E. & Mandrone, G., 2013. Integration of 3D geological modeling and gravity surveys for geothermal prospection in an Alpine Region, *Tectonophysics,* **608,** 1025–1036.

Häring, M., 2001. Technischer Bericht Geothermie-Sondierbohrung Otterbach 2, Basel, Geothermal Explorers Ltd, available at: www.bfe.admin.ch (last accessed 15 January 2014).

Illies, H.J. & Greiner, G., 1979. Holocene movements and state of stress in the rhinegraben rift system, *Tectonophysics,* **52,** 349–359.

Klemperer, S.L., 1987. A relation between continental heat flow and the seismic reflectivity of the lower crust, *J. Geophys.,* **61,** 1–11.

Klingelé, E. & Schwendener, H., 1984. *Geophysikalisches Untersuchungsprogramm Nordschweiz: Gravimetrische Messungen 81/82,* Nagra, Baden.

Kohl, T., Bächler, D. & Rybach, L., 2000. Steps towards a comprehensive thermo-hydraulic analysis of the HDR test site Soultz-sous- Forêts, in *Proceedings of the World Geothermal Congress 2000,* Kyushu-Tohoku, Japan, May–June 2000, pp. 2671–2676.

Laubscher, H., 1965. Ein kinematisches Modell der Jurafaltung, *Eclogae geol. Helv.,* **54,** 2221–2282.

Mann, P., Hempton, M.R., Bradley, D.C. & Burke, K., 1983. Development of pull-apart basins, *J. Geol.,* **91,** 529–554.

Marchant, R., Ringgenberg, Y., Stampfli, G., Birkhäuser, P., Roth, P. & Meier, B., 2005. Paleotectonic evolution of the Zürcher Weinland (northern Switzerland), based on 2D and 3D seismic data, *Eclogae geol. Helv.,* **98,** 345–362.

Matter, A., 1987. Faciesanalyse und Ablagerungsmilieus des Permokarbons im Nordschweizer Trog, *Eclogae geol. Helv.,* **80,** 345–367.

Matter, A., Peters, T., Bläsi, H.-R., Meyer, J., Ischi, H. & Meyer, C., 1988a. Sondierbohrung Weiach—Geologie, Nagra *Technischer Bericht,* NBT 90-04, Baden.

Matter, A., Peters, T., Bläsi, H.-R., Schenker, F. & Weiss, H.P., 1988b. Sondierbohrung Schafisheim—Geologie, Nagra Textband und Beilagenband, NTB 86-03, Baden.

Matter, A., Peters, T., Isenschmid, C., Bläsi, H.-R. & H.-J. Ziegler, 1987. Sondierbohrung Riniken—Geologie, Nagra *Technischer Bericht, NBT* 86–02, Baden.

McCann, T. *et al.*, 2006. Post-Variscan (end Corboniferous-Early Permian) basin evolution in Western and Central Europe, *Geol. Soc., Lond. Memoirs,* **32,** 355–388.

Muksin, U., Haberland, C., Bauer, K. & Weber, M., 2013. Three-dimensional upper crustal structure of the geothermal system in Tarutung (North Sumatra, Indonesia) revealed by seismic attenuation tomography, *Geophys. J. Int.,* **195,** 2037–2049.

Müller, M., Nieberding, F. & Wanninger, A., 1988. Tectonic style and pressure distribution at the northern margin of the Alps between Lake Constance and the River Inn, *Geol Rundsch,* **77,** 787–796.

NAGRA, 2008. Vorschlag geologischer Standortgebiete für das SMA- und das HAA-Lager—Geologische Grundlagen, Technischer Bericht 08-04, ed. Nagra. Nagra, Wettingen.

Peters, T., Matter, A., Bläsi, H.R. & Gautschi, A., 1986. Sondierbohrung Böttstein–Geologie, Nagra Textband und Beilagenband, NTB, Baden.

Peters, T., Matter, A., Bläsi, H.R., Isenschmid, C., Kleboth, P., Meyer, C. & Meyer, J., 1989a. Sondierbohrung Leuggern—Geologie, Nagra Textband und Beilagenband, NTB.

Peters, T., Matter, A., Meyer, J., Isenschmid, C. & Ziegler, H.J., 1989b. Sondierbohrung Kaiseten—Geologie, Nagra Textband und Beilagenband, NTB, Baden.

Pfiffner, O.A., 2009. *Geologie der Alpen,* 1st edn, Haupt Verlag.

Pfiffner, O.A., Erard, P. & Stäuble, M., 1997. Two cross sections through the Swiss Molasse Basin (lines E4-E6, W1, W7-W10), in *Deep Structure of the Swiss Alps: Results of NRP 20,* pp. 64–72, eds Pfiffner, O.A., Lehner, P., Heitzmann, P., Müller, S. & Steck, A. Birkhäuser.

Pohanka, V., 1988. Optimum expression for computation of the gravity field of a homogeneous polyhedral body, *Geophys. Prospect.,* **36,** 733–751.

Pribnow, D. & Schellschmidt, R., 2000. Thermal tracking of upper crustal fluid flow in the Rhine Graben, *Geophys. Res. Lett.,* **27,** 1957–1960.

Rybach, L., Eugster, W. & Griesser, J.C., 1987. Die geothermischen Verhaeltnisse in der Nordschweiz, *Eclogae geol. Helv.,* **80,** 521–534.

Sailhac, P., Galdeano, A., Gibert, D., Moreau, F. & Delor, C., 2000. Identification of sources of potential fields with the continuous wavelet transform: complex wavelets and application to aeromagnetic profiles in French Guiana, *J. geophys. Res.,* **105,** 19 455–19 475.

Schill, E. & Klingler, P., 2010. Increase of productivity in the Riehen geothermal system (Switzerland): tracer test and reservoir, *Mitteilungen der Geotechnik Schweiz,* **161,** 35–40.

Schill, E., Guglielmetti, L., Klingler, P., Abdelfettah, Y. & Alcolea, A., 2012. The role of structural changes for geothermal projects in the area of Basel, in *Proceedings of the Thirty-Seventh Workshop on Geothermal Reservoir Engineering,* Stanford University, Stanford, California, January 30 - February 1, 2012, SGP-TR-194.

Schumacher, M.E., 2002. Upper Rhine Graben: role of preexisting structures during rift evolution, *Tectonics,* **21,** 1–17.

Sommaruga, A., Eichenberger, U. & Marillier, F., 2012. Seismic Atlas of the Swiss Molasse Basin, *Matér. Géol. Suisse, Géophys.,* **44,** 1–88.

Swisstopo, 2005a. Geologische Karte der Schweiz. Karte 1:500 000, *Bundesamt für Landestopografie swisstopo,* Wabern.

Swisstopo, 2005b. Tektonische Karte der Schweiz. Karte 1:500 000, *Bundesamt für Landestopografie swisstopo,* Wabern.

Swisstopo, 2005c. DHM25-The digital height model of Switzerland. 15S., Federal Office for Topography Swisstopo, Wabern, 1–15.

Ustaszewski, K. & Schmid, S.M., 2007. Latest Pliocene to recent thick-skinned tectonics at the Upper Rhine Graben—Jura Mountains junction, *Swiss J. Geosci.,* **100,** 293–312.

Ustaszewski, K., Schumacher, M.E. & Schmid, S.M., 2005. Simultaneous normal faulting and extensional flexuring during rifting: an example from the southernmost Upper Rhine Graben, *Int. J. Earth Sci.,* **94,** 680–696.

Vollmayr, T. & Wendt, A., 1987. Die Erdgasbohrung Entlebuch-1, ein Tiefenaufschluss am Alpennordrand, *Bull. Assoc. Suisse Géol. Ing. Pétrole,* **53**(125), 67–79.

Wessel, P., Smith, W.H.F., Scharroo, R., Luis, J.F. & Wobbe, F., 2013. Generic mapping tools: improved version released, *EOS, Trans. Am. geophys. Un.,* **94,** 409–410.

Zeh, A. & Brätz, H., 2004. Timing of Upper Carboniferous-Permian horst-basin formation and magmatism in the NW Thuringian Forest, central Germany: a review. *Geol. Soc., Lond., Spec. Publ.,* **223**(1), 319–334.

Ziegler, P.A., 1990. Collision related intra-plate compression deformations in Western and Central Europe, *J. Geodyn.,* **11,** 357–388.

Ziegler, P.A., 1992. Swiss Molasse Basin—Geodynamics, Resources, Hazards—an introduction, *Eclogae geol. Helv.,* **85,** 511–517.